Parametric Sensitivity Analysis and Design Optimization of an Interior Permanent Magnet Synchronous Motor

HAO CHEN[1,2], (Member, IEEE), AND CHRISTOPHER H. T. LEE[1], (Senior Member, IEEE)

[1]School of Electrical and Electronic Engineering, Nanyang Technological University, Singapore 639798
[2]School of Automation, Beijing Institute of Technology, Beijing 100081, China

Corresponding author: Christopher H. T. Lee (chtlee@ntu.edu.sg)

ABSTRACT Due to the advantages of high torque density, high efficiency, and wide constant power speed range (CPSR), interior permanent magnet synchronous motors (IPMSMs) are gaining more and more attention in electric vehicle (EV) applications. There are many geometrical parameters in IPMSMs, and some of them have significant impact on the performance of such machines. This paper presents a parametric sensitivity study of the rotor geometrical parameters for a V-shaped magnet IPMSM. In which, both the individual sensitivity and the combined sensitivity with considering the interaction effects of these parameters are performed by finite-element analysis (FEA). The electromagnetic characteristics in the low-speed range, including average torque, torque ripple, cogging torque, power density, power factor, efficiency, *etc.* and the flux-weakening capability in the high-speed range are investigated in detail. Based on the parametric study, the V-shaped magnet IPMSM is optimized. The results show that the performance of the optimal design is significantly improved. In addition, the validity of the FEA simulation results is verified by experiment with a prototype.

INDEX TERMS Design optimization, interior permanent magnet synchronous motor, parametric sensitivity analysis.

I. INTRODUCTION

With the increased concerns on the energy shortage and environment pollution, traditional vehicles equipped with internal combustion engine (ICE) are facing serious challenges due to their pollutant emissions. By contrast, electric vehicles (EVs) have been widely regarded as one of the most promising solutions to solve the problems associated with ICE vehicles [1].

In EVs, motors are the unique source for propulsion. The motors for EVs require both good torque characteristics in the low-speed range and good flux-weakening capability in the high-speed range [2], [3]. In the last few decades, many different kinds of motors have been developed for EV applications [4]–[13]. Due to the low reliability caused by mechanical commutators and brushes, DC motors have been replaced by AC motors [5]. In AC motors, induction machines are used in this application due to the advantages of high reliability and low cost. However, this type of motor

consists of a number of drawbacks, such as low efficiency, low power factor, and low inverter-usage factor, especially in the high-speed range [6]. Permanent magnet (PM) brushless motors are more capable than induction machines, and they have been adopted by many famous automakers due to the merits of high efficiency, high power factor, high power density, *etc.* [7], [8]. There are various configurations of PM brushless motors. For instance, PM retention is needed in surface-mounted PM motors in the high-speed range and this limits their applications. Moreover, they suffer from high risk of irreversible demagnetization, since the PMs face to the armature field directly [9]. Flux-switching PM motors have been gaining interests due to their novel structure in a sense that both armature windings and PMs are located on the stator. They exhibit wide constant power speed region (CPSR) and good mechanical integrity, which are suitable for high-speed application. However, the low PM material utilization in flux-switching PM motors would increase the cost significantly [10]. In order to meet the requirements in both the low-speed range and the high-speed range simultaneously, interior permanent magnet synchronous motors (IPMSMs)

The associate editor coordinating the review of this manuscript and approving it for publication was Cheng Qian.

whose PMs are embedded in the rotor are considered to be very promising candidates [11]–[13].

In order to obtain better comprehensive performance, many optimal designs by optimizing the geometrical parameters in IPMSMs have been reported in many other literatures [14]–[20]. In [14], Jannot *et al.* presented an optimal design for a spoke-type IPMSM. It is shown that eight out of thirteen geometrical parameters, *e.g.*, the PM width, have more significant impact on the objective function of the weight of the machine than the others. In [15], Barcaro *et al.* investigated the influence of rotor geometry on the stator iron losses for a two-layer tangential-type IPMSM. It is shown that the stator iron losses could be limited only if a proper design of the rotor flux-barrier angles is made. In [16], Kim *et al.* optimized the torque characteristics of a tangential-type IPMSM based on the ratio of pole-arc to pole-pitch and saliency due to duct structures. It is found that both the pole-arc to pole-pitch ratio and duct structures are important design parameters for torque characteristics of the investigated IPMSM. In [17], Han *et al.* presented an optimal rotor design for a triangle-type IPMSM. It is shown that high torque and low torque ripple are simultaneously achieved by optimizing the insert position of the PMs. In [18], Kano investigated the torque ripple reduction techniques for IPMSMs. It is shown that the torque ripple is dramatically reduced from 35% to 7% by changing the PM shape from a tangential-type IPMSM to a V-shaped IPMSM with a novel flux barrier design. In [19], Kim *et al.* presented a design optimization process for a V-shaped IPMSM with the genetic algorithm method. It is shown that the flux-weakening rate (L_q/L_d) is increased by 26%, which indicates that the flux-weakening capability in the high-speed range is significantly improved, through optimizations of the flux barrier shape and the inserted PM position. Accordingly, a V-shaped IPMSM is investigated in this paper. All of these aforementioned literatures indicate that the rotor geometrical parameters have significant impacts on the performance characteristics of IPMSMs, and the performance could be improved through ingenious rotor structure optimization. However, there are very few technical papers with a methodological parametric study before optimization. The methodological parametric study is necessary because there is a high degree of freedom when determining the geometrical parameters and the knowledge of geometrical parameters is particularly important during the optimization process [20].

In [21], Amoros *et al.* presented a consistent sensitivity analysis of the influence of several geometrical parameters, such as the stator-pole length, the translator-pole length, the stack length, the yoke length, and the air-gap length, on the performance of a linear switched reluctance motor. It shows that how the motor performances, *e.g.*, the average force, are affected by these parameters. It can then provide a guideline for the optimal design of the linear switched reluctance motors. In [22], Bianchi *et al.* presented a sensitivity analysis of torque ripple reduction of a three-layer tangential-type IPMSM. Then, the highly influential geometrical parameters

are selected to be involved in the optimization in order to achieve a high and smooth output torque. However, only the torque characteristics are taken into account in the mentioned paper, while other performance characteristics especially the performance in the high-speed range are neglected. Moreover, most of the existing parametric sensitivity analyses for IPMSM are individual parametric analyses, while the interaction effects of the investigated parameters are not taken into account.

Differing from the previous works, this paper brings new contributions by presenting a comprehensive parametric sensitivity analysis of a V-shaped IPMSM. The influences of the rotor geometrical parameters on the performance of the investigated IPMSM in both the low- and high-speed ranges are investigated in detail. These rotor geometrical parameters include the angle between the two V-shaped PMs under each pole, the magnetic barrier, the PM parameters, *etc*. The comprehensive parametric sensitivity analysis includes both the individual sensitivity and the combined sensitivity with considerations on the interaction effects of these parameters. The sensitivity analysis study would be helpful for designers/engineers to select geometrical variables with significant influence on motor performances, as well as choose reasonable ranges for each geometrical variable. This study would be much more meaningful if the sequential subspace optimization method is used in large-scale optimization of IPMSMs in order to reduce the computational burden. As a result, the whole parameters are divided into several subspaces based on their significant order, and then these subspaces are optimized sequentially [23], [24]. Moreover, based on the parametric analysis study, the design optimization of the investigated IPMSM with the design of experiment (DOE) method is provided.

The parametric analysis study and design optimization of the investigated V-shaped IPMSM focus on the main performance characteristics in both the low- and high-speed ranges, *viz.* the torque characteristics, the power density, the power factor, the efficiency, *etc*. in the low-speed range and the flux-weakening capability in the high-speed range. The electromagnetic interference (EMI) level as discussed in [25]–[27], the modulation technique and the switching frequency operation in [28], are beyond the scope of this paper while these materials will be substance of our future work.

II. INITIALLY DESIGNED IPMSM
The investigated IPMSM with V-shaped PMs is shown in Fig. 1. The specifications of this motor are listed in Table 1.

A. OPERATING PRINCIPLE OF IPMSMS
The knowledge of the operating principle of IPMSMs is of importance for the design of such machines.

The trajectory of the current vector for the control strategies of the IPMSM machines is depicted in Fig. 2(a). When the motor is running below the base speed, the maximum torque-per-ampere (MTPA) control mode is applied for the maximum output torque. The current limit locus is a circle
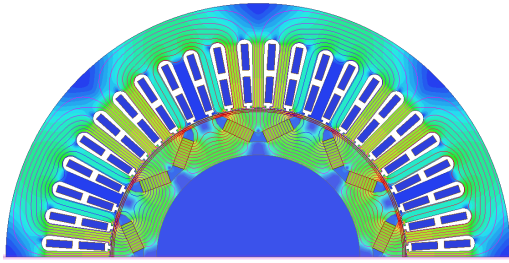
FIGURE 1. Cross-sectional view of the IPMSM.

TABLE 1. Specifications of the IPMSM.

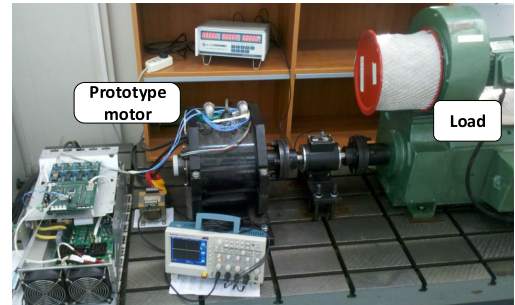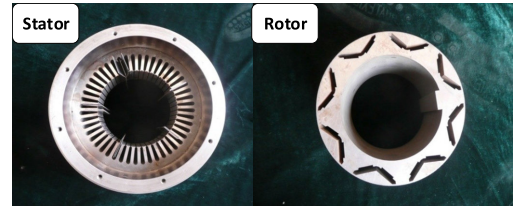| Design parameter	Value
Rated voltage limit (VAC)	77
Rated current limit (A)	60
Number of poles/slots	8/48
Outer diameter of stator (mm)	275
Axial length of stator core (mm)	83
Air-gap length (mm)	0.75
Material of PM	NdFeB (B_r=1.29T, H_c=987kA/m)

FIGURE 2. (a) The trajectory of the current vector of IPMSMs. (b) Phasor diagram of IPMSMs.

while the voltage limit locus is an ellipse. The operation area of the motor is within the intersection of the current limit circle and the voltage limit ellipse [29]. The maximum output will be located at point A, where the speed is the base speed. When the speed increases from ω_1 to ω_2, the motor will be operated at point B if the MTPA mode is still applied, where the current is less than the limit current, i_{lim}. It means a low utilization ratio of the power converter. Hence, in order to increase the maximum output power, the flux-weakening control mode should be applied by changing the current leading angle, γ, as shown in Fig. 2(b). The output power at

FIGURE 3. Prototype of the IPMSM with V-shape PMs.

point C [see Fig. 2(a)] could be obtained which is higher than that of point B. Based on the aforementioned discussions, it can be inferred that the IPMSM should be controlled by MTPA mode below the base speed and by flux-weakening control mode above the base speed. Hence, the performance requirements for the design of IPMSMs include not only good torque characteristics in the low-speed range but also good flux-weakening capability in the high-speed range. The electromagnetic torque, T_e, is expressed by eq. (1). It consists of two parts, *i.e.* the magnet torque derived from PM and the reluctance torque due to the difference between d- and q-axis inductances. The base speed, n_b, is expressed by eq. (2).

$$T_e = p[\psi_m i_s \cos\gamma + 1/2\left(L_d - L_q\right) i_s^2 \sin 2\gamma]$$
$$= p[\psi_m i_q + \left(L_d - L_q\right) i_d i_q] \quad (1)$$
$$n_b = \frac{60}{2\pi} \frac{u_{\lim}}{p\sqrt{(\psi_m - L_d i_d)^2 + \left(L_q i_q\right)^2}} \quad (2)$$

where, p is the number of rotor pole pairs, ψ_m is the PM flux linkage, i_s is the phase current, L_d, L_q, i_d, i_q are the d- and q-axis inductances and currents, u_{lim} is the limit voltage.

B. INITIAL MOTOR MODEL AND EXPERIMENTAL VALIDATION

A prototype of an IPMSM with V-shaped PMs is manufactured without comprehensive optimization, as shown in Fig. 3. More details can be found in [30]. The simulated and measured results of back-electromotive force (EMF) are shown in Fig. 4. The torque and power versus speed are shown in Fig. 5. It is found that the simulation results based on the finite-element analysis (FEA) are in good agreement with the experimental results. All of these experimental results have verified the effectiveness of the FEA-based simulation method. Hence, it is reliable to use the FEA-based simulation method to further investigate the IPMSM in this paper.
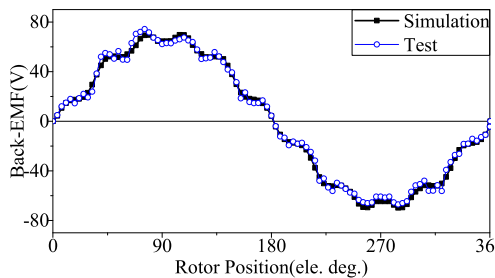
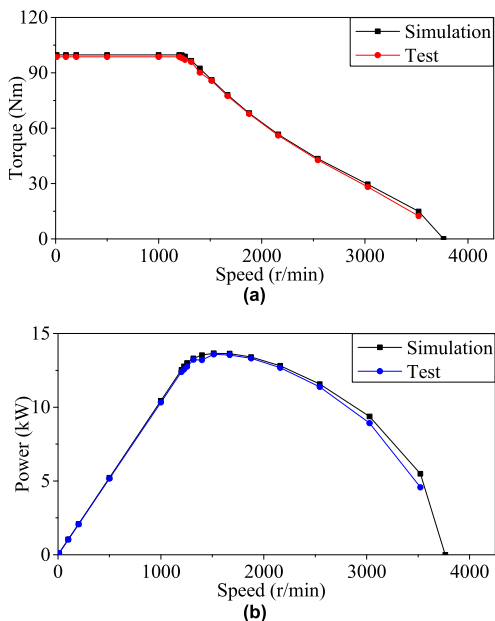**FIGURE 4.** Comparison of no-load phase back-EMF.

FIGURE 5. (a) Torque vs. speed. (b) Power vs. speed.

On the other hand, it can be seen that there are abundant higher-order harmonic components in the back-EMF waveform, which indicates high torque ripple and high losses. In addition, the CPSR is not wide enough which means that the flux-weakening capability in the high-speed range needs to be improved. Thus, this motor should be further optimized. Before the optimization, sensitivity analysis of geometrical parameters is necessary to be carried out.

III. INDIVIDUAL SENSITIVITY ANALYSIS OF GEOMETRICAL PARAMETERS ON PERFORMANCE OF THE IPMSM

The individual sensitivity analysis of rotor geometrical parameters in this IPMSM is investigated in this section. There is a high degree of freedom when determining the rotor geometrical parameters. Due to the flux-focusing effects, the V-shaped PM rotor of the IPMSM helps to concentrate the magnetic flux to rotor surface. Since the angle between the two PMs under each pole determines the magnetic circuit structure in both d- and q-axis, the angle between the two PMs is a key geometrical parameter. Small width of magnetic barrier can reduce magnetic flux leakage, but it also reduces
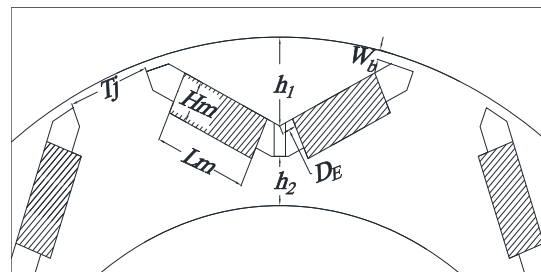

FIGURE 6. Geometrical parameters of the IPMSM.

the mechanical strength, especially in the high-speed range. Therefore, an appropriate value of the magnetic barrier width should be chosen. In addition, since the PM is the source of magnetomotive force that determines the magnetic loading of the motor, the position of the PMs and the shape of PM, $e.g.$, the thickness and length of PM are also key parameters of the IPMSM. Therefore, six rotor geometrical parameters, as depicted in Fig. 6 are selected to be investigated in this paper, namely the duct depth ratio ($h^* = h_1/h_2$), the rib ratio ($T_j^* = T_j/\tau$, τ is polar pitch), the width of magnetic barrier (W_b), the embedded depth of PM (D_E), the thickness and length of PMs (H_m and L_m). It should be noted that when one of them varies, the others are fixed.

A. ANGLE BETWEEN TWO PMS-H*

To be measured more accurately, the angle between the two PMs under each pole is represented by the duct depth ratio h^*, and the angle decreases with h^* increasing. In the low-speed range, the IPMSM for EV applications should have sufficient average torque, T_{avg}, to provide enough driving force for climbing or acceleration; low cogging torque, T_{cog}, and low torque ripple, T_{ripple}, to reduce acoustic noise and vibration; high power factor, P_f, to increase utilization ratio of the power converter; high efficiency to save energy. Hence, the mentioned performance characteristics of the motor are investigated, obtained, and compared, with different h^* at the base speed. All these results are summarized and listed in Table 2. It should be noted that in order to explain how the geometrical parameter affects these performance characteristics, the flux leakage coefficient, σ_0, the PM flux linkage, ψ_m, and the total harmonic distortion of the no-load back-EMF, THD, are also listed in this table.

It shows that as h^* increases, the flux leakage coefficient σ_0 increases, while the PM flux linkage ψ_m, average torque T_{avg}, cogging torque T_{cog}, and torque ripple T_{ripple} decrease. The THD becomes the minimum 7.68% at h^* being 1.0. The power factor P_f, power density P/v, and efficiency η become the maximum 0.93, 7.60 MW/m^3, and 96.73%, respectively, at h^* being 0.5. It can be explained according to the basic PM machine electromagnetic field theory as that with h^* increasing, the d-axis magnetic circuit becomes narrow, and the distance between the PMs and the air-gap increases, more flux leakage occurs and the effective magnetic

TABLE 2. Performance characteristics of the motor with different $h*$.

h^*	0.5	1.0	1.5	2.0	2.5	3.0
n_b(rpm)	1190	1195	1208	1212	1209	1225
σ_0	1.205	1.216	1.224	1.230	1.234	1.237
ψ_m(Wb)	0.115	0.114	0.113	0.112	0.111	0.110
T_{avg}(Nm)	101.63	100.26	99.44	98.65	98.03	97.37
T_{cog}(Nm)	7.53	5.50	5.09	4.85	4.72	4.65
THD(%)	8.93	7.68	7.89	8.12	8.43	8.65
T_{ripple}(%)	16.48	15.04	13.66	12.83	12.37	11.83
P_f	0.93	0.92	0.92	0.92	0.91	0.92
P/v(MW/m^3)	7.60	7.53	7.54	7.52	7.45	7.50
η (%)	96.73	96.71	96.72	96.70	96.68	96.70

TABLE 3. Performance characteristics of the motor with different T_j^*.

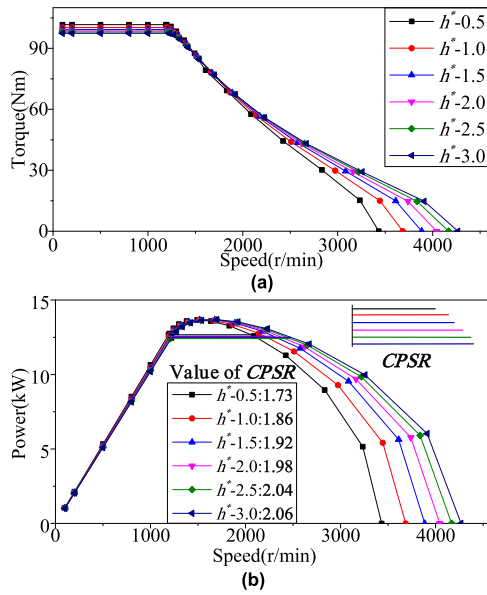| T_j^*	0.10	0.15	0.20	0.25	0.30	0.35
n_b(rpm)	1247	1231	1214	1201	1192	1181
σ_0	1.252	1.237	1.230	1.226	1.224	1.223
ψ_m(Wb)	0.104	0.108	0.111	0.112	0.114	0.115
T_{avg}(Nm)	93.50	96.14	98.06	99.67	100.75	101.30
T_{cog}(Nm)	3.38	3.85	1.98	6.00	7.42	3.43
THD(%)	10.49	6.55	7.12	8.67	11.15	16.61
T_{ripple}(%)	10.05	6.02	9.47	14.92	11.43	3.71
P_f	0.897	0.910	0.915	0.943	0.923	0.919
P/v(MW/m^3)	7.34	7.44	7.48	7.71	7.55	7.52
η (%)	96.63	96.68	96.69	96.70	96.69	96.63

FIGURE 7. Flux-weakening capability with different $h*$. (a) Torque vs. speed. (b) Power vs. speed.

FIGURE 8. Flux-weakening capability with different T_j^*. (a) Torque vs. speed. (b) Power vs. speed.

energy decreases. Thus, the flux leakage coefficient increases and the average torque decreases.

The flux-weakening performance including the torque and power versus speed at the limit current is shown in Fig. 7. It should be noted that the CPSR is evaluated by the ratio of the higher speed (the right point of line segment) to the base speed (the left point of line segment) in Fig. 7 (b), in which the powers of the two points are the same. As can be seen, the CPSR increases with h^* increasing.

B. ANGLE BETWEEN TWO PMS-T_{J*}

The angle between the two PMs can also be described by the rib ratio T_j^* as shown in Fig. 6, in which h^* is fixed and the angle will decrease with T_j^* increasing. The performance characteristics of the motor with different T_j^* at the base speed are listed in Table 3.

It shows that as T_j^* increases, the flux leakage coefficient σ_0 decreases, while the PM flux linkage ψ_m and average torque T_{avg} increase. The cogging torque T_{cog}, THD, and torque ripple T_{ripple} become the minimum 1.98Nm, 6.55%, and 3.71% at T_j^* being 0.20, 0.15, and 0.35, respectively, while the power factor P_f, power density P/v, and
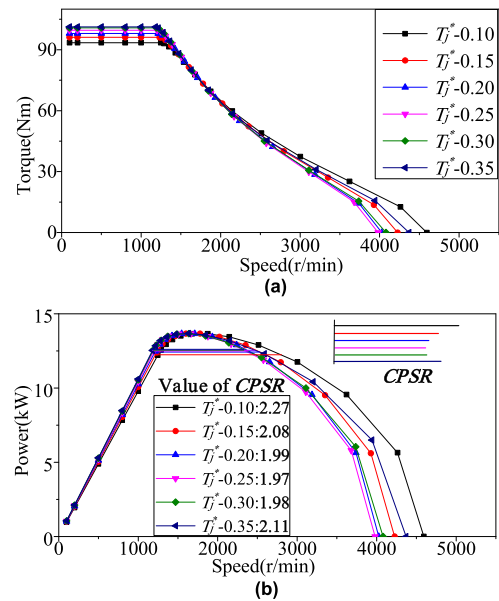
efficiency η become the maximum 0.943, 7.71 MW/m^3, and 96.70% at T_j^* being 0.25. The average torque increases due to the fact that the flux leakage decreases and the effective magnetic energy increases.

The flux-weakening performance is shown in Fig. 8. As can be seen, with T_j^* increasing, the CPSR decreases first and then increases.

C. WIDTH OF MAGNETIC BARRIER

The performance characteristics of the motor with different width of magnetic barrier W_b at the base speed are listed in Table 4.
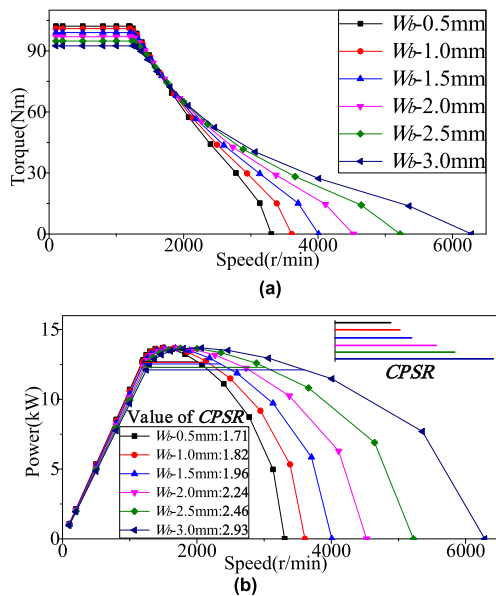
It shows that as W_b increases, the flux leakage coefficient σ_0 increases, while the PM flux linkage ψ_m, average torque T_{avg}, power factor P_f, power density P/v, and efficiency η decrease. The cogging torque T_{cog}, THD, and torque ripple T_{ripple} become the minimum 2.40 Nm, 7.74%, and 9.63% at W_b being 0.5 mm, 2.0 mm, and 0.5 mm, respectively. The reason is that with W_b increasing, the magnetic reluctance of leakage magnetic circuit decreases, serious flux leakage occurs and hence the effective magnetic energy decreases.

TABLE 4. Performance characteristics of the motor with different W_b.

W_b(mm)	0.5	1.0	1.5	2.0	2.5	3.0
n_b(rpm)	1185	1196	1209	1210	1237	1249
σ_0	1.113	1.169	1.231	1.300	1.384	1.475
ψ_m(Wb)	0.120	0.116	0.112	0.107	0.102	0.097
T_{avg}(Nm)	102.19	101.00	99.02	96.96	94.84	92.53
T_{cog}(Nm)	2.40	3.38	4.52	4.38	4.02	3.53
THD(%)	8.87	8.76	8.09	7.74	8.60	10.27
T_{ripple}(%)	9.63	11.93	13.07	13.23	11.97	10.22
P_f	0.929	0.925	0.920	0.902	0.901	0.888
P/v(MW/m^3)	7.60	7.56	7.52	7.38	7.37	7.26
η (%)	96.74	96.73	96.71	96.65	96.64	96.60

TABLE 5. Performance characteristics of the motor with different D_E.

D_E (mm)	2	3	4	5	6	7
n_b(rpm)	1214	1209	1202	1209	1205	1203
σ_0	1.239	1.235	1.230	1.226	1.221	1.217
ψ_m(Wb)	0.11194	0.11192	0.11190	0.11187	0.11182	0.11173
T_{avg}(Nm)	98.41	98.66	98.95	99.08	99.06	99.06
T_{cog}(Nm)	4.26	4.34	4.42	4.49	4.55	4.64
THD(%)	7.90	7.91	8.01	8.14	8.35	8.85
T_{ripple}(%)	11.01	11.83	12.20	13.57	14.56	15.43
P_f	0.918	0.917	0.915	0.919	0.918	0.916
P/v(MW/m^3)	7.51	7.50	7.48	7.52	7.50	7.49
η (%)	96.71	96.70	96.69	96.72	96.70	96.69

FIGURE 9. Flux-weakening capability with different W_b. (a) Torque vs. speed. (b) Power vs. speed.

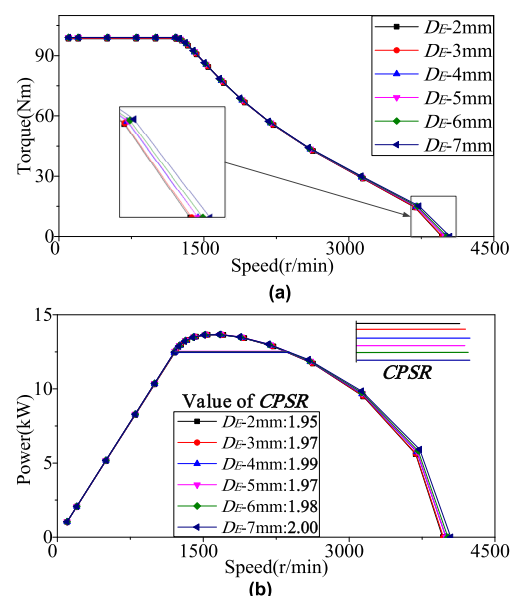**FIGURE 10.** Flux-weakening capability with different D_E. (a) Torque vs. speed. (b) Power vs. speed.

The flux-weakening performance is shown in Fig. 9. As can be seen, the CPSR increases with W_b increasing.

D. EMBEDDED DEPTH OF PM

The performance characteristics of the motor with different embedded depth of PM D_E at the base speed are listed in Table 5.

It shows that as D_E increases, the flux leakage coefficient σ_0 and PM flux linkage ψ_m decrease, while the cogging torque T_{cog}, THD, and torque ripple T_{ripple} increase. The average torque T_{avg}, power factor P_f, power density P/v, and efficiency η become the maximum 99.08 Nm, 0.919, 7.52 MW/m^3, and 96.72% at D_E being 5mm, respectively. It can be seen that the decrease of the PM flux linkage seems contradictory to the decrease of the flux leakage. The reason is that with D_E increasing, the distance between the two PMs of each pole increases, the magnetic flux-focusing effects and the PM utilization ratio decrease.

The flux-weakening performance is shown in Fig. 10. As can be seen, the variation of D_E has little impact on the CPSR of this machine.

E. THICKNESS OF PM

The performance characteristics of the motor with different thickness of PM H_m at the base speed are listed in Table 6.

It shows that as H_m increases, the PM flux linkage ψ_m, cogging torque T_{cog}, power factor P_f, power density P/v, and efficiency η increase. The flux leakage coefficient σ_0, THD, and torque ripple T_{ripple} become the minimum 1.220, 7.80%, and 10.90% at H_m being 5 mm, 4 mm, and 4 mm, respectively. The average torque T_{avg} becomes the maximum 99.41 Nm at H_m being 8 mm. The average torque does not increase all along with H_m increasing because the PMs are series connected in the d-axis magnetic circuit. Even though the magnetomotive force produced by PMs and the effective magnetic energy increase, the magnetic reluctance of the d-axis magnetic circuit increases since the magnetic reluctance of the PM is much higher than that of the silicon steel.

The flux-weakening performance is shown in Fig. 11. As can be seen, the CPSR decreases with H_m increasing.

TABLE 6. Performance characteristics of the motor with different H_m.

H_m(mm)	4	5	6	7	8	9
n_b(rpm)	1233	1215	1211	1203	1209	1223
σ_0	1.244	1.220	1.226	1.230	1.233	1.236
ψ_m(Wb)	0.104	0.110	0.111	0.112	0.113	0.114
T_{avg}(Nm)	92.55	97.15	98.58	99.32	99.41	98.80
T_{cog}(Nm)	0.22	4.27	4.41	4.50	4.56	4.60
THD(%)	7.80	8.09	8.02	7.96	7.93	7.96
T_{ripple}(%)	10.90	13.31	13.16	13.07	12.74	12.10
P_f	0.878	0.906	0.917	0.918	0.922	0.928
P/v(MW/m³)	7.18	7.41	7.50	7.51	7.54	7.59
η (%)	96.56	96.66	96.70	96.71	96.72	96.73
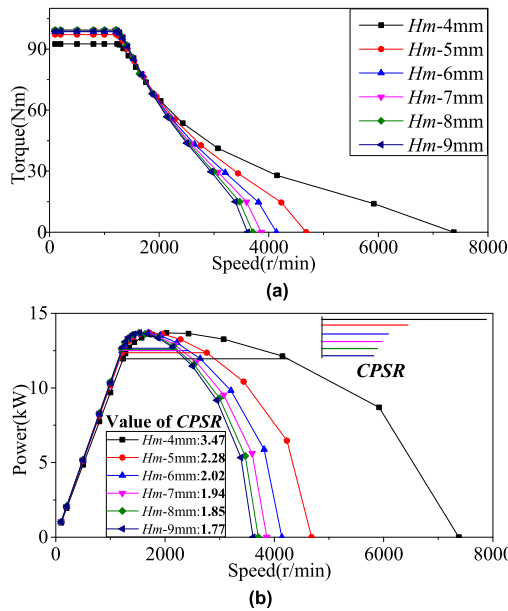
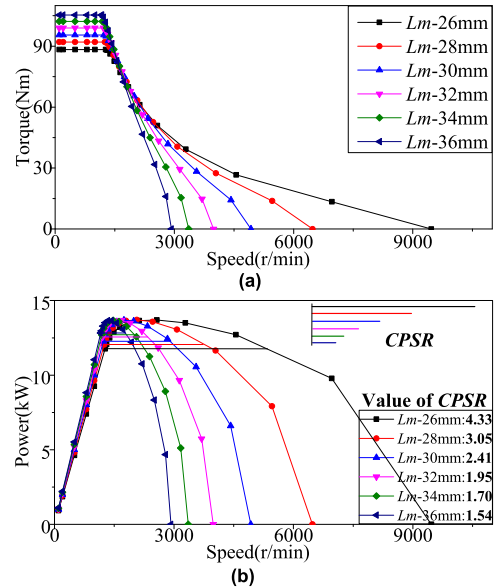**FIGURE 11.** Flux-weakening capability with different H_m. (a) Torque vs. speed. (b) Power vs. speed.

TABLE 7. Performance characteristics of the motor with different L_m.

L_m (mm)	26	28	30	32	34	36
n_b(rpm)	1272	1250	1226	1211	1186	1162
σ_0	1.300	1.273	1.249	1.228	1.210	1.195
ψ_m(Wb)	0.088	0.096	0.104	0.112	0.119	0.126
T_{avg}(Nm)	88.37	92.07	95.52	99.01	102.25	105.38
T_{cog}(Nm)	2.68	3.18	3.76	4.46	5.52	7.15
THD(%)	8.57	8.30	8.06	8.01	8.76	11.01
T_{ripple}(%)	11.01	11.07	11.86	13.10	14.72	16.09
P_f	0.86	0.88	0.90	0.92	0.93	0.94
P/v(MW/m³)	7.07	7.23	7.36	7.53	7.62	7.69
η (%)	96.51	96.59	96.64	96.71	96.74	96.76

F. LENGTH OF PM

The performance characteristics of the motor with different length of PM L_m at the base speed are listed in Table 7.

It shows that as L_m increases, the flux leakage coefficient σ_0 decreases, while the PM flux linkage ψ_m, average torque T_{avg}, cogging torque T_{cog}, torque ripple T_{ripple}, power factor P_f, power density P/v, and efficiency η increase. The THD becomes the minimum 8.01% at L_m being 32 mm.

FIGURE 12. Flux-weakening capability with different L_m. (a) Torque vs. speed. (b) Power vs. speed.

TABLE 8. Weighting set for multi-objective optimal design.

	T_{avg}	T_{ripple}	T_{cog}	η	CPSR
λ_i	0.3	0.1	0.05	0.15	0.4

TABLE 9. Individual sensitivity analysis results.

SS_i	T_{avg}	T_{ripple}	T_{cog}	η	CPSR	$F(x)_{multi}$
h^*	0.029	0.237	0.554	0.001	0.116	0.106
T_j^*	0.072	1.247	1.946	0.002	1.144	0.701
W_b	0.050	0.202	0.473	0.002	0.344	0.197
D_E	0.006	0.362	0.073	0.001	0.067	0.068
H_m	0.062	0.152	0.518	0.002	0.691	0.336
L_m	**0.547**	**1.482**	**3.113**	**0.008**	**3.706**	**1.952**

The reason is that with L_m increasing, the magnetic field strength and effective magnetic energy increase.

The flux-weakening performance is shown in Fig. 12. As can be seen, the CPSR decreases with L_m increasing.

G. RESULTS ANALYSIS AND DISCUSSION

The influence of the six rotor geometrical parameters on the performance of the V-shaped IPMSM in the both low- and high-speed ranges are investigated in this section. These parameters affect the magnetic circuit and the effective magnetic energy. Hence, the variation of these parameters will affect the performance of the IPMSM. However, the sensitivities of these six rotor geometrical parameters to the performance of this machine are different. Hence, an individual sensitivity analysis study of these geometrical parameters is performed based on the results obtained above.

For a comprehensive study, the performance characteristics including the average torque, torque ripple, cogging torque, and efficiency at the base speed, as well as the flux-weakening

TABLE 10. Experimental results of objective function.

Exp.	h^*	T_j^*	W_b	D_E	H_m	L_m	T_{avg}(Nm)	T_{ripple}(%)	T_{cog}(Nm)	η (%)	CPSR
1	1	1	1	1	1	1	80.16	15.16	2.22	96.34	2.96
2	1	2	2	2	2	2	91.39	10.79	1.94	96.60	2.52
3	1	3	3	3	3	3	97.27	12.07	3.92	96.67	2.03
4	1	4	4	4	4	4	100.20	14.41	7.50	96.71	2.07
5	1	5	5	5	5	5	101.50	8.74	9.09	96.73	1.80
6	1	6	6	6	6	6	104.69	11.26	13.17	96.75	1.50
7	2	1	2	3	4	5	99.54	8.37	3.45	96.70	1.64
8	2	2	3	4	5	6	104.27	1.54	2.98	96.75	1.44
9	2	3	4	5	6	1	87.17	9.51	2.34	96.74	4.33
10	2	4	5	6	1	2	84.42	11.55	2.72	96.27	8.59
11	2	5	6	1	2	3	90.04	4.83	3.69	96.36	4.75
12	2	6	1	2	3	4	105.07	19.62	13.77	96.73	1.46
13	3	1	3	4	5	6	101.38	8.21	4.22	96.68	1.57
14	3	2	4	5	6	1	84.43	4.62	1.15	96.30	4.82
15	3	3	5	6	1	2	82.25	9.68	1.57	96.15	9.32
16	3	4	6	1	2	3	87.88	6.82	1.80	96.30	5.06
17	3	5	1	2	3	4	104.09	15.88	10.33	96.67	1.51
18	3	6	2	3	4	5	109.01	16.99	10.23	96.72	1.35
19	4	1	4	5	6	2	84.91	9.08	2.35	96.35	3.89
20	4	2	5	6	1	3	81.46	4.00	1.84	96.08	8.10
21	4	3	6	1	2	4	89.66	8.60	2.76	96.37	3.45
22	4	4	1	2	3	5	105.56	12.75	6.16	96.64	1.50
23	4	5	2	3	4	6	110.07	18.44	16.41	96.63	1.33
24	4	6	3	4	5	1	89.08	4.66	1.03	96.30	4.92
25	5	1	5	6	2	3	84.83	6.22	2.08	96.23	5.13
26	5	2	6	1	3	4	88.32	3.65	1.85	96.22	3.13
27	5	3	1	2	4	5	103.50	5.89	8.07	96.58	1.58
28	5	4	2	3	5	6	107.78	15.28	10.51	96.57	1.38
29	5	5	3	4	6	1	86.54	10.44	4.46	96.26	4.26
30	5	6	4	5	1	2	83.48	2.30	2.12	96.05	8.93
31	6	1	6	2	3	4	86.50	5.78	1.49	96.26	3.50
32	6	2	1	3	4	5	101.30	11.45	6.89	96.53	1.67
33	6	3	2	4	5	6	105.01	8.21	3.93	96.53	1.48
34	6	4	3	5	6	1	86.35	12.51	3.08	96.24	4.20
35	6	5	4	6	1	2	83.37	11.50	3.62	96.04	8.74
36	6	6	5	1	2	3	85.14	5.45	4.37	96.16	5.55

capability in the high-speed range are set as optimization objectives. The optimization model is defined by eq. (3) [see the bottom of this page], where the subscript *initial* means the corresponding values of the initial prototype as described in section II. The CPSR is a key evaluation index for motors used in EVs applications especially in the high-speed range. The average torque is also important when climbing as well as accelerating in the low-speed range. Hence, the CPSR and average torque are weighted more than the other objectives. The weighted

$$
\begin{aligned}
\max : &F(\mathrm{x})_{multi} \\
= &\lambda_1 \frac{T_{avg}}{T_{avg\_initial}} + \lambda_2 \frac{T_{ripple\_initial}}{T_{ripple}} \\
&+ \lambda_3 \frac{T_{cog\_initial}}{T_{cog}} + \lambda_4 \frac{\eta}{\eta_{initial}} + \lambda_5 \frac{CPSR}{CPSR_{initial}}
\end{aligned} \tag{3}
$$

coefficient λ_i is set based on the engineering experience and the specific requirements of the investigated motor-drive system, which is listed in Table 8.

In order to make the sensitivity results of these geometrical parameters comparable, the sensitivity results are normalized since different parameters have different units. The sensitivity results are obtained based on eq. (4).

$$
SS = \frac{1}{k} \sum_{i=1}^{k} \left| \frac{\partial y_i(x)/y(x)_{initial}}{\partial x_i/x_{initial}} \right| \tag{4}
$$

where, $y(x)$ is the value of the objective, x is the value of the geometrical parameter, k is the number of experiments.

The individual sensitivity analysis results of the geometrical parameters of the investigated IPMSM are listed in Table 9. It can be seen that the length of PM L_m has the most significant impact on the objectives, including the average torque, torque ripple, cogging torque, efficiency, and CPSR. For the objective function as expressed in eq. (3), the sensitivity order of the six investigated geometrical parameters is,

$$
L_m > T_j^* > H_m > W_b > h^* > D_E \tag{5}
$$

TABLE 11. Combined sensitivity analysis results.

SS_i	T_{avg}	T_{ripple}	T_{cog}	η	$CPSR$	$F(x)_{multi}$
h^*	0.197	1.005	0.502	0.011	3.606	1.628
T_j^*	0.223	1.021	1.500	0.013	4.377	1.997
W_b	0.732	**4.931**	4.026	**0.034**	8.736	4.414
D_E	0.228	1.146	2.066	0.009	2.623	1.337
H_m	0.344	1.207	3.525	0.014	3.330	1.734
L_m	**0.982**	3.279	**5.836**	0.029	**11.575**	**5.549**

IV. COMBINED SENSITIVITY ANALYSIS OF GEOMETRICAL PARAMETERS ON PERFORMANCE OF THE IPMSM

It should be noted that when one of the six geometrical parameters varies, the others are fixed during the anlysis in section III. Hence, the interaction effects of these parameters are neglected. However, it is imperative to take into account the interaction effects among these geometrical parameters in the actual motor design, since the neglection of the interaction effects will lead to a non-comprehensive optimal design in the optimization.

The design of experiments (DOE) is a statistical method whose validity has been verified in analysis of experiments. There are six levels for each geometrical parameter as presented in section III. Hence, 46, 656 (6^6) case-studies need to be investigated for a conventional full-factor design, while orthogonal arrays can dramatically reduce the number of experiments, meanwhile, gain the maximum amount of information [31], [32]. Accordingly, the DOE method with orthogonal arrays is used in this section in order to reduce the computational burden.

The experimental analysis results of the $L_{36}(6^6)$ matrix using FEA are listed in Table 10. The numbers 1 to 6 in this matrix are the levels of each parameter, e.g., the level 1 value of the parameter h^* is 0.5, the level 6 value of the parameter T_j^* is 0.35.

Based on the DOE results, the sensitivity results of these geometrical parameters are also calculated by eq. (4), in which $y_i(x)$ is the mean value of the specific objective at level i. The combined sensitivity analysis results of the geometrical parameters with taking into account the interaction effects of these geometrical parameters are listed in Table 11.

As can be seen, the most sensitive parameters for the average torque, torque ripple, cogging torque, efficiency, and CPSR are L_m, W_b, L_m, W_b, and L_m, respectively. For the objective function as expressed in eq. (3), the sensitivity order of the six investigated geometrical parameters is,

$$L_m > W_b > T_j^* > H_m > h^* > D_E \qquad (6)$$

As can be seen, there is a difference between the individual sensitivity analysis results presented in section III and the combined sensitivity analysis results in this section. It should be noted that this difference mentioned above should be highlighted in the design and/or optimization of the IPMSM, otherwise, the comprehensive/synthetic optimal design might not be obtained.

TABLE 12. *SN* results for each objective function.

Exp.	$SN(T_{avg})$	$SN(T_{ripple})$	$SN(T_{cog})$	$SN(\eta)$	$SN(CPSR)$
1	38.08	-23.61	-6.93	39.68	9.43
2	39.22	-20.66	-5.76	39.70	8.03
3	39.76	-21.63	-11.87	39.71	6.15
4	40.02	-23.17	-17.50	39.71	6.32
5	40.13	-18.83	-19.17	39.71	5.11
6	40.40	-21.03	-22.39	39.71	3.52
7	39.96	-18.45	-10.76	39.71	4.30
8	40.36	-3.75	-9.48	39.71	3.17
9	38.81	-19.56	-7.38	39.71	12.73
10	38.53	-21.25	-8.69	39.67	18.68
11	39.09	-13.68	-11.34	39.68	13.53
12	40.43	-25.85	-22.78	39.71	3.29
13	40.12	-18.29	-12.51	39.71	3.92
14	38.53	-13.29	-1.21	39.67	13.66
15	38.3	-19.72	-3.92	39.66	19.39
16	38.88	-16.68	-5.11	39.67	14.08
17	40.35	-24.02	-20.28	39.71	3.58
18	40.75	-24.60	-20.20	39.71	2.61
19	38.58	-19.16	-7.42	39.68	11.80
20	38.22	-12.04	-5.30	39.65	18.17
21	39.05	-18.69	-8.82	39.68	10.76
22	40.47	-22.11	-15.79	39.70	3.52
23	40.83	-25.32	-24.30	39.70	2.48
24	39.00	-13.37	-0.26	39.67	13.84
25	38.57	-15.88	-6.36	39.67	14.20
26	38.92	-11.25	-5.34	39.67	9.91
27	40.30	-15.40	-18.14	39.70	3.97
28	40.65	-23.68	-20.43	39.70	2.80
29	38.74	-20.37	-12.99	39.67	12.59
30	38.43	-7.23	-6.53	39.65	19.02
31	38.74	-15.24	-3.46	39.67	10.88
32	40.11	-21.18	-16.76	39.69	4.45
33	40.42	-18.29	-11.89	39.69	3.41
34	38.73	-21.95	-9.77	39.67	12.46
35	38.42	-21.21	-11.17	39.65	18.83
36	38.60	-14.73	-12.81	39.66	14.89

V. OPTIMIZATION RESULTS AND DISCUSSION

In this section, the design optimization of the V-shaped IPMSM is carried out and discussed based on the aforementioned sensitivity analysis results. In order to perform the design optimization, two kinds of signal-to-noise ratio SN are adopted as expressed in eq. (7) and eq. (8), respectively [33]. Eq. (7) is the larger-the-better characteristic for the objectives of the average torque, efficiency, and CPSR, while eq. (8) is the smaller-the-better characteristic for the objectives of the torque ripple and cogging torque. The calculated SN results based on the DOE results as presented in section III, are listed in Table 12. For a reasonable comparison, the SN results are normalized as expressed in eq. (9). Then, the synthetic SN is calculated by eq. (10) with the weighted coefficients λ_i as listed in Table 8.

$$SN = -10\log_{10}(1/y^2) \qquad (7)$$

$$SN = -10\log_{10}(y^2) \qquad (8)$$

$$norm(SN) = (SN - \overline{SN})/s.d.(SN) \qquad (9)$$

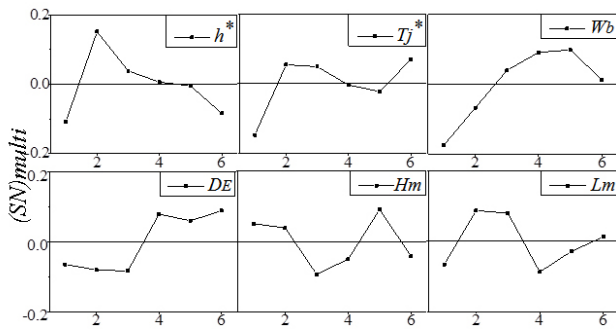$$(SN)_{multi} = \sum_{i=1} \lambda_i \cdot norm(SN) \qquad (10)$$

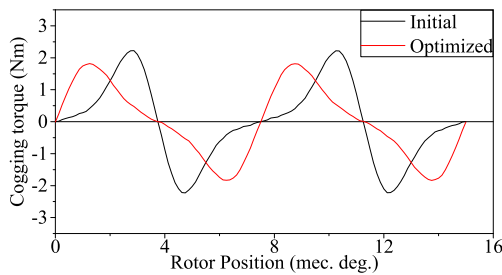**FIGURE 13.** Main effect analysis as a result of the design optimization.

FIGURE 14. Comparison results of cogging torque.

TABLE 13. Initial and optimized design variables.

Variables	h^*	T_j^*	W_b(mm)	D_E(mm)	H_m(mm)	L_m(mm)
Initial	1.8	0.23	1.48	4.5	6.48	32
Optimized	1.0	0.35	2.5	7	8	28

where, y is the value of the experiment results as listed in Table 10, $\overline{SN}$ is the mean value of SN, $s.d(SN)$ is the standard deviation of SN.

The main effect plot for the synthetic SN is shown in Fig. 13. To obtain better synthetic/comprehensive optimal performance, the variable levels that indicate higher $(SN)_{multi}$ should be selected. Therefore, the optimized design variables are selected and listed in Table 13.

Fig. 14 shows the comparison results of cogging torque of the V-shaped IPMSM before and after optimization, while Fig. 15 shows the comparison results of flux-weakening capability. The performance characteristics in terms of the five objectives of the initially designed IPMSM and the optimal motor are listed in Table 14. In addition, the total material cost for the initially designed prototype and the optimal design candidate motor are 75.05 and 76.81, respectively. The cost function is expressed by eq. (11), in which the ferromagnetic materials of the stator and rotor are set up as the base/unity value for all materials and the cost ratios are selected as typical values for high volume production [10].

$$Cost = 24 \cdot m_{PM} + 3 \cdot m_{Cu} + 1 \cdot m_{Fe} \qquad (11)$$

where, m_{PM}, m_{Cu}, and m_{Fe} are the masses of the PM, copper windings, and the ferromagnetic material of the stator and rotor, respectively.
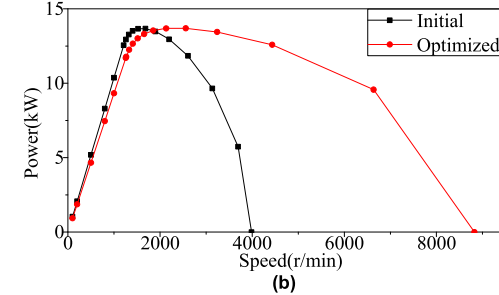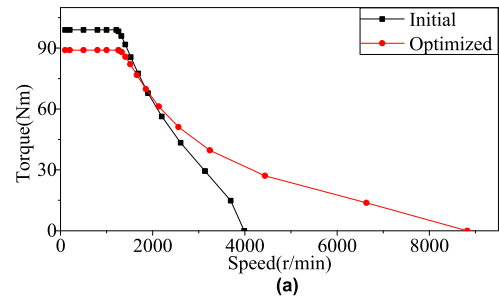

FIGURE 15. Comparison results of flux-weakening capability. (a) Torque vs. speed. (b) Power vs. speed.

TABLE 14. Objective function results.

	T_{avg}(Nm)	T_{ripple}(%)	T_{cog}(Nm)	η(%)	CPSR	$F(x)_{multi}$
Initial	99.01	13.10	4.46	96.72	1.95	1
Optimized	89.05	8.36	3.66	96.60	3.56	1.36

As can be seen, the synthetic objective function results the optimal design as 1.36, which has been significantly improved by 36% compared to the initially designed prototype. On the other hand, the material cost of the optimal design is only 2.35% higher than that of the initially designed prototype.

VI. CONCLUSION

The prototype of the V-shaped IPMSM without comprehensive optimization was manufactured, while the optimal design has not been assembled. The simulation results and experimental results of the initially designed motor are in good agreement. Hence, the validity of the FEA simulation method is verified.

The individual sensitivity analysis of the six geometrical parameters the V-shaped IPMSM are investigated in this paper. The individual sensitivity analysis results provide guidelines for designers/engineers in the design of the V-shaped IPMSMs for EV applications. In particular, the performance characteristics are very sensitive to some of these geometrical parameters but insensitive to some of the others. Although both of the parameters h^* and T_j^* define the angle between the two PMs under each pole and the angle decreases with h^* and T_j^* increasing, the influence of these two parameters on the performance characteristics of the motor are quite different. In general, smaller h^* and W_b, larger T_j^* and L_m, and appropriate values of H_m indicate better performance characteristics in the low-speed range. Meanwhile smaller H_m and L_m, larger h^* and W_b, and an appropriate value of T_j^* indicate better flux-weakening capability in the high-speed

range. In addition, the D_E has little impact on the performance characteristics of this motor.

In order to consider the interaction effects of these geometrical parameters, the combined sensitivity analysis of these geometrical parameters of the motor is investigated based on DOE and orthogonal arrays techniques. Moreover, five objectives, *viz.* the average torque, torque ripple, cogging torque, efficiency, and CPSR are set in the design optimization of this motor. The results show that there is a difference between the individual and combined sensitivity analysis results for the synthetic objective function, *i.e.*, $L_m > T_j^* > H_m > W_b > h^* > D_E$ for the individual sensitivity analysis, while $L_m > W_b > T_j^* > H_m > h^* > D_E$ for the combined sensitivity analysis.

The design optimization of the investigated V-shaped IPMSM is presented based on the aforementioned parametric analysis results. The synthetic objective function of the optimal motor is significantly improved by 36% compared to the initially designed prototype.

REFERENCES

[1] F. Li, K. T. Chau, and C. Liu, "Pole-changing flux-weakening DC-excited dual-memory machines for electric vehicles," *IEEE Trans. Energy Convers.*, vol. 31, no. 1, pp. 27–36, Mar. 2016.

[2] M. Zeraoulia, M. E. H. Benbouzid, and D. Diallo, "Electric motor drive selection issues for HEV propulsion systems: A comparative study," *IEEE Trans. Veh. Technol.*, vol. 55, no. 6, pp. 1756–1764, Nov. 2006.

[3] R. Dutta, L. Chong, and M. F. Rahman, "Design and experimental verification of an 18-Slot/14-pole fractional-slot concentrated winding interior permanent magnet machine," *IEEE Trans. Energy Convers.*, vol. 28, no. 1, pp. 181–190, Mar. 2013.

[4] K. T. Chau, C. C. Chan, and C. Liu, "Overview of permanent-magnet brushless drives for electric and hybrid electric vehicles," *IEEE Trans. Ind. Electron.*, vol. 55, no. 6, pp. 2246–2257, Jun. 2008.

[5] L. Chang, "Recent developments of electric vehicles and their propulsion systems," *IEEE Aerosp. Electron. Syst. Mag.*, vol. 8, no. 12, pp. 3–6, Dec. 1993.

[6] A. Haddoun, M. E. H. Benbouzid, D. Diallo, R. Abdessemed, J. Ghouili, and K. Srairi, "Modeling, analysis, and neural network control of an EV electrical differential," *IEEE Trans. Ind. Electron.*, vol. 55, no. 6, pp. 2286–2294, Jun. 2008.

[7] T. A. Burress, "Evaluation of the 2010 toyota prius hybrid synergy drive system," Oak Ridge Nat. Lab., Oak Ridge, TN, USA, Tech. Rep. ORNL/TM-2010/253, 2011.

[8] *Electric Motors 101: Understanding the Basics of Electric Motor Technology*. General Motors Company, Detroit, MI, USA. Accessed: Oct. 2011. [Online]. Available: https: media.gm.com/content/Pages/news/us/en/2011/Oct/1026_spark_elec_mtr/_jcr_content/iconrow/textfile/file.res/Electric_Motors_101.pdf

[9] G. Pellegrino, A. Vagati, P. Guglielmi, and B. Boazzo, "Performance comparison between surface-mounted and interior PM motor drives for electric vehicle application," *IEEE Trans. Ind. Electron.*, vol. 59, no. 2, pp. 803–811, Feb. 2012.

[10] H. Chen, X. Liu, N. A. O. Demerdash, A. M. EL-Refaie, Z. Chen, and J. He, "Computationally efficient optimization of a five-phase flux-switching PM machine under different operating conditions," *IEEE Trans. Veh. Technol.*, vol. 68, no. 7, pp. 6495–6508, Jul. 2019.

[11] X. Lu, K. L. V. Iyer, K. Mukherjee, and N. C. Kar, "Investigation of integrated charging and discharging incorporating interior permanent magnet machine with damper bars for electric vehicles," *IEEE Trans. Energy Convers.*, vol. 31, no. 1, pp. 260–269, Mar. 2016.

[12] K. Kiyota and A. Chiba, "Design of switched reluctance motor competitive to 60-kW IPMSM in third-generation hybrid electric vehicle," *IEEE Trans. Ind. Appl.*, vol. 48, no. 6, pp. 2303–2309, Nov./Dec. 2012.

[13] K. Chen, Y. Sun, and B. Liu, "Interior permanent magnet synchronous motor linear field-weakening control," *IEEE Trans. Energy Convers.*, vol. 31, no. 1, pp. 159–164, Mar. 2016.

[14] X. Jannot, J.-C. Vannier, C. Marchand, M. Gabsi, J. Saint-Michel, and D. Sadarnac, "Multiphysic modeling of a high-speed interior permanent-magnet synchronous machine for a multiobjective optimal design," *IEEE Trans. Energy Convers.*, vol. 26, no. 2, pp. 457–467, Jun. 2011.

[15] M. Barcaro, N. Bianchi, and F. Magnussen, "Rotor flux-barrier geometry design to reduce stator iron losses in synchronous IPM motors under FW operations," *IEEE Trans. Ind. Appl.*, vol. 46, no. 5, pp. 1950–1958, Sep./Oct. 2010.

[16] K.-C. Kim, D.-H. Koo, J.-P. Hong, and J. Lee, "A study on the characteristics due to pole-arc to pole-pitch ratio and saliency to improve torque performance of IPMSM," *IEEE Trans. Magn.*, vol. 43, no. 6, pp. 2516–2518, Jun. 2007.

[17] J.-H. Han, J. Lee, and W.-H. Kim, "A study on optimal design of the triangle type permanent magnet in IPMSM rotor by using the Box–Behnken design," *IEEE Trans. Magn.*, vol. 51, no. 3, pp. 1–4, Mar. 2015.

[18] Y. Kano, "Torque ripple reduction of saliency-based sensorless drive concentrated-winding IPMSM using novel flux barrier," *IEEE Trans. Ind. Appl.*, vol. 51, no. 4, pp. 2905–2916, Jul. 2015.

[19] J. B. Kim, K. Y. Hwang, and B. I. Kwon, "Optimization of two-phase in-wheel IPMSM for wide speed range by using the Kriging model based on Latin hypercube sampling," *IEEE Trans. Magn.*, vol. 47, no. 5, pp. 1078–1081, May 2011.

[20] R. Mujal-Rosas and J. Orrit-Prat, "General analysis of the three-phase asynchronous motor with spiral sheet rotor: Operation, parameters, and characteristic values," *IEEE Trans. Ind. Electron.*, vol. 58, no. 5, pp. 1799–1811, May 2011.

[21] J. G. Amoros and P. Andrada, "Sensitivity analysis of geometrical parameters on a double-sided linear switched reluctance motor," *IEEE Trans. Ind. Electron.*, vol. 57, no. 1, pp. 311–319, Jan. 2010.

[22] N. Bianchi, M. Degano, and E. Fornasiero, "Sensitivity analysis of torque ripple reduction of synchronous reluctance and interior PM motors," *IEEE Trans. Ind. Appl.*, vol. 51, no. 1, pp. 187–195, Jan. 2015.

[23] G. Lei, T. Wang, Y. Guo, J. Zhu, and S. Wang, "System-level design optimization methods for electrical drive systems: Deterministic approach," *IEEE Trans. Ind. Electron.*, vol. 61, no. 12, pp. 6591–6602, Dec. 2014.

[24] G. Lei, W. Xu, J. Hu, J. Zhu, Y. Guo, and K. Shao, "Multilevel Design Optimization of a FSPMM Drive System by Using Sequential Subspace Optimization Method," *IEEE Trans. Magn.*, vol. 50, no. 2, pp. 685–688, Feb. 2014.

[25] K. Gulez and A. A. Adam, "High-frequency common-mode modeling of permanent magnet synchronous motors," *IEEE Trans. Electromagn. Compat.*, vol. 50, no. 2, pp. 423–426, May 2008.

[26] T. Rahimi, S. Y. khangah, and B. Yousefi, "Reduction EMI due to di/dt and dv/dt DC and AC sides of BLDC motor drive," in *Proc. 5th Annu. Int. Power Electron., Drive Syst. Technol. Conf. (PEDSTC)*, Feb. 2014, pp. 428–433.

[27] N. Mousavi, T. Rahimi, and H. M. Kelk, "Reduction EMI of BLDC motor drive based on software analysis," *Adv. Mater. Sci. Eng.*, vol. 2016, Jan. 2016, Art. no. 1497360. [Online]. Available: https://www.hindawi.com/journals/amse/2016/1497360/

[28] X. Ding, G. Liu, M. Du, H. Guo, C. Duan, and H. Qian, "Efficiency improvement of overall PMSM-inverter system based on artificial bee colony algorithm under full power range," *IEEE Trans. Magn.*, vol. 52, no. 7, Jul. 2016, Art. no. 8106904.

[29] F. Parasiliti, M. Villani, S. Lucidi, and F. Rinaldi, "Finite-element-based multiobjective design optimization procedure of interior permanent magnet synchronous motors for wide constant-power region operation," *IEEE Trans. Ind. Electron.*, vol. 59, no. 6, pp. 2503–2514, Jun. 2012.

[30] X. Liu, H. Chen, J. Zhao, and A. Belahcen, "Research on the performances and parameters of interior PMSM used for electric vehicles," *IEEE Trans. Ind. Electron.*, vol. 63, no. 6, pp. 3533–3545, Jun. 2016.

[31] H. M. Hasanien, A. S. Abd-Rabou, and S. M. Sakr, "Design optimization of transverse flux linear motor for weight reduction and performance improvement using response surface methodology and genetic algorithms," *IEEE Trans. Energy Convers.*, vol. 25, no. 3, pp. 598–605, Sep. 2010.

[32] G. Lei, C. Liu, J. Zhu, and Y. Guo, "Techniques for multilevel design optimization of permanent magnet motors," *IEEE Trans. Energy Convers.*, vol. 30, no. 4, pp. 1574–1584, Dec. 2015.

[33] K.-C. Kim, J. Lee, H. J. Kim, and D.-H. Koo, "Multiobjective optimal design for interior permanent magnet synchronous motor," *IEEE Trans. Magn.*, vol. 45, no. 3, pp. 1780–1783, Mar. 2009.
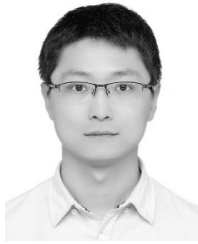
HAO CHEN (M'19) received the B.Sc. degree in electrical engineering from the School of Electrical Engineering, Beijing Jiaotong University, Beijing, China, in 2012, and the Ph.D. degree in control science and engineering from the School of Automation, Beijing Institute of Technology, Beijing, in 2019.

From 2016 to 2018, he was with the Department of Electrical and Computer Engineering, Marquette University, Milwaukee, WI, USA, as a Joint Ph.D. Student. He is currently a Postdoctoral Research Fellow with the School of Electrical and Electronic Engineering, Nanyang Technological University, Singapore. His research interests include design and optimization of electric machines, power electronic drives, and motor control.

CHRISTOPHER H. T. LEE (M'12–SM'18) received the B.Eng. (Hons.) and Ph.D. degrees in electrical engineering from the Department of Electrical and Electronic Engineering, The University of Hong Kong, Hong Kong.

He is currently an Assistant Professor with the School of Electrical and Electronic Engineering, Nanyang Technological University, Singapore, a Visiting Assistant Professor with the Massachusetts Institute of Technology, USA, and an Honorary Assistant Professor in his alma mater. His research interests include electric machines and drives, renewable energies, and electric vehicle technologies. In these areas, he has published one book, three books chapters, and about 70 refereed articles.

Dr. Lee received many awards, including the Nanyang Assistant Professorship, the Li Ka Shing Prize (the best Ph.D. thesis prize), and the Croucher Foundation Fellowship to support his postdoctoral research. He is also an Associate Editor of IEEE Access and *IET Renewable Power Generation*.

• • •